

# High Sensitivity Infrared Extended Wavelength Response InGaAs Detectors

Matthew J. Nelson, Michael F. Skrutskie, Srikrishna Kanneganti and Chan Park  
University of Virginia, 530 McCormick Rd., Charlottesville, VA 22904 USA

## ABSTRACT

Recent development of low dark current  $2.34\ \mu\text{m}$ -cutoff InGaAs material has resulted in the successful construction of a hybrid focal plane array built on the SB-206  $512\times 512$  format astronomical quality Read Out Integrated Circuit (ROIC). This contribution reports on the verification of the quality of the InGaAs material as well as the essential characteristics and performance of the hybrid focal plane array. The results of the investigation indicate that the dark current levels surpass the requirements for ground-based broadband and narrowband imaging as well as for low resolution spectroscopy in the astronomical H and  $K_s$  bands.

**Keywords:** InGaAs, infrared arrays

## 1. INTRODUCTION

The 1980's saw the introduction of InSb and HgCdTe detectors for civilian applications and infrared-sensitive detectors have ever since been in use for astronomical applications. However, near-infrared detector arrays are still prohibitively costly for most small telescope facilities and for wide-field applications even at large facilities.

By contrast, infrared detectors based on InGaAs technology are less costly, but development and applications to date have been primarily for high signal level, high background applications, although  $1.7\ \mu\text{m}$ -cutoff InGaAs arrays have been developed for space astronomy.<sup>1,2</sup> These applications typically do not require detector operability at wavelengths longer than the standard  $1.7\ \mu\text{m}$  cutoff characteristic of lattice-matched InGaAs on InP substrates, and interest in developing low-background InGaAs detectors with extended-wavelength cutoffs out to  $2.5\ \mu\text{m}$  has lagged. Such detectors would be of keen interest to astronomers who regularly exploit the  $2.0$ - $2.4\ \mu\text{m}$  atmospheric (K-band) window, however the lattice mismatch of this material to InP substrates produces significant dark current which can overwhelm ground-based backgrounds. Specifically, observations in the K-band (as well as the  $1.5$ - $1.8\ \mu\text{m}$  H-band) from the ground are background limited by airglow and thermal emission such that dark currents as high as a  $1000\ e^-/s/pixel$  can be tolerated<sup>3,4</sup> for pixels that are scaled to  $0.25''$ - $0.5''$  on the sky.

Research<sup>5</sup> has indicated that stacked buffer layers of slowly changing  $\text{In}_x\text{Ga}_{1-x}\text{As}$  built on the InP substrate can minimize lattice strain and thus mitigate dark current which can be as high as  $10^4\ e^-/s/pixel$  for  $20\ \mu\text{m}$  pixels<sup>6</sup> in traditional extended-wavelength InGaAs growths on InP. Overall, extended wavelength response detectors would be most useful at much colder operating temperatures than the standard InGaAs detectors, but their operability and behavior at cryogenic temperatures is largely unexplored.

The infrared instrumentation laboratory at the University of Virginia has engaged in an NSF-funded collaboration with Goodrich Sensors Unlimited, Inc. (GSU), a leader in InGaAs applications technology, to develop and characterize improved extended wavelength response InGaAs material. Previously,<sup>7</sup> we have reported on the successful fabrication of detector material which surpasses the above-mentioned dark current requirements for astronomical applications. The performance of the original ROICs for these earlier studies limited the characterization of these arrays at cryogenic temperatures. A next natural step was to create hybrids with an astronomically proven low-noise cryogenic ROIC. This paper presents analysis of a detector array based on the new extended-wavelength InGaAs material hybridized to a Raytheon SB-206 astronomical quality ROIC, and describes future plans to exercise this device in a rigorous astronomical application.

---

Further author information: Send correspondence to M.N.: E-mail: mjn4n@virginia.edu, Telephone: 1-434-924-4906

## 2. EXPERIMENTAL SETUP

Testing of this array occurred in a cryogenic and optical configuration nearly identical to the one used in previous tests of InGaAs detectors at the University of Virginia.<sup>7</sup> The readout electronics, however, were entirely different since the SB-206 requires substantially more complex clocking than the previous generation of GSU arrays tested in this program.

### 2.1 The Array

The detector array consists of a  $512 \times 512$  array of extended-wavelength  $\text{In}_{0.83}\text{Ga}_{0.17}\text{As}$  photodiodes, indium bump bonded to one quadrant of a Raytheon SB-206 Silicon Cryo-CMOS ROIC<sup>8</sup> which is mounted on a 100-pin Kyocera ceramic leadless chip carrier. The SB-206 is used in 1- and 4-quadrants mode with the popular Aladdin Infrared arrays produced by Ratheon Vision Systems. The pixel pitch of the array is  $27\mu\text{m} \times 27\mu\text{m}$  pixels, with a source-follower-per-detector input circuit, and consists of a reset switch transistor, a read-out switch transistor and a PMOS driver transistor that acts as a unity gain source follower. The x-y addressing circuit consists of two (fast and slow) CMOS multiplexer circuits which read out sets of 8 pixels at a time to the 8 output lines. The ROIC allows for a readout time as short as  $67\text{ms}$ .

### 2.2 Electronics

The implementation of this array with a low noise ROIC meant a switch from a Labview based system used previously to a more flexible high accuracy set of clocking and readout electronics. The one quadrant SB-206 consists of 8 outputs and 22 clock and bias lines, and is substantially more complicated to operate than the SU ROIC previously used. For the testing of this array an Astronomical Research Cameras(ARC) GenIII<sup>9</sup> system with a single 8 channel ARC-46 IR video processor board was used to provide sufficient accuracy and dynamic range in the readout of the array. The software to operate the system was also provided by ARC. The array is run with the clock at 200kHz giving a pixel address time of  $5\mu\text{s}$  and a readout time of  $340\text{ms}$  in a doubly-correlated sampling mode.

### 2.3 Cryogenics

The cryogenic setup for array testing consists of a cryostat with an anti-reflection coated infrasil window for illumination with calibration sources. The vacuum vessel contains a thermally-isolated 9-inch diameter aluminum cold plate attached to the cold head of a closed-cycle Cryotiger cooling system. The cooling system has the capacity to dissipate 5W at an operating temperature of 80K. From room temperature the system requires 42 hours to reach 80K. Under good vacuum the system requires 40 hours to reach room temperature after the cryogenic refrigerator is turned off.

### 2.4 Optical Setup

A flat screen that covered the entire external viewing field of the array provided illumination for linearity testing and estimation of the array flat field. For quantum efficiency measurements an optical reimaging system relayed the pinhole exit aperture of a monochromator onto the array or onto an InAs reference diode. The exit pinhole of the monochromator is re-imaged to about  $300\mu\text{m}$  to avoid edge effects when used with the InAs diode, which has diameter of  $500\mu\text{m}$ .

The monochromator is an Optometrics model SDMC1-01G with an integral stepping motor, with a step increment of 0.5nm and is configured to provide a wavelength resolution of 2nm. Reset and control of wavelength is done by manual setting for the array measurements and by software control of the motor for the diode measurements. The imaging system consists of a spherical mirror and a flat mirror as shown in Figure 2. The light source and monochromator are mounted on an XYZ stage for control of the position of the resulting pinhole image. Along the light path to the fold mirror a filter provides order blocking for the monochromator, and an aperture is used to limit the focal ratio and control aberrations in the image. This setup was designed to allow the testing of the original diodes as reported by Nelson(2006).<sup>7</sup>

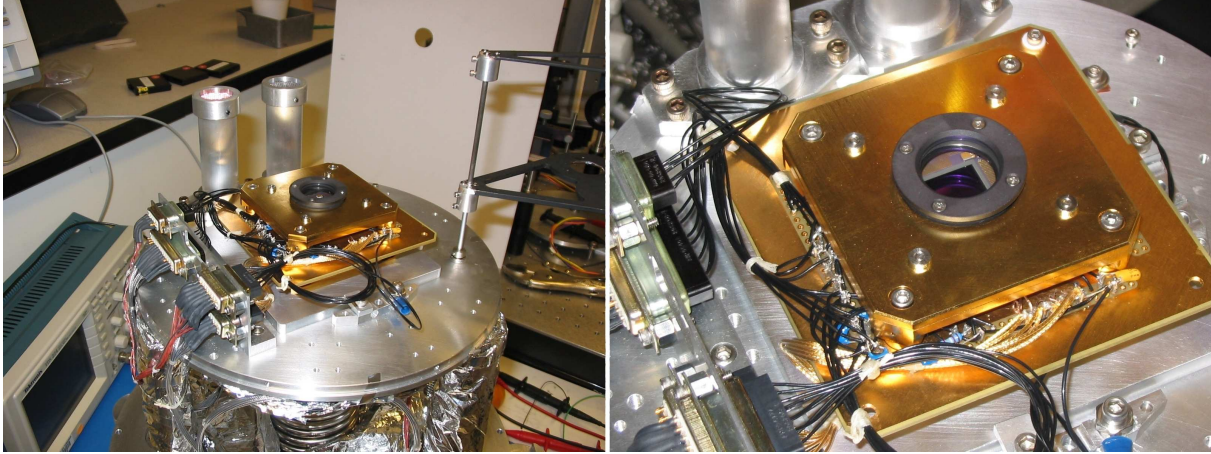


Figure 1. The cryogenic configuration for testing the InGaAs array. The coils of the cold-head of the closed-cycle cooling system can be seen below the work plate in the picture on the left. A radiation shield covers the work plate and isolates the detector for testing. The flaps on the right can be moved into position to block off the external light if needed. Dark-testing involves covering the aperture atop the detector mount shown in the picture on the right with metal tape.

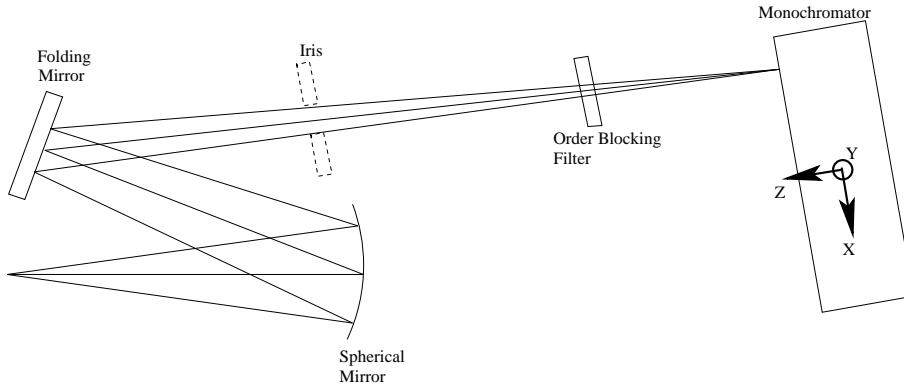


Figure 2. A schematic of the imaging system for focusing light from the exit aperture of the monochromator on the array and the calibration diode.

### 3. ANALYSIS

#### 3.1 Pixel Response Distribution

Figure 3 shows the relative response of the pixels of the array. The image was corrected for gradients in illumination from the flat field using 2nd-order polynomials in both directions. The variation in the response has a full-width half-maximum of about 8%.

#### 3.2 Pixel Yield

The raw response of the array to a moderately good flat field is shown in Figure 4. About 95% of the pixels have a similar response. Another 4% of the pixels form peculiar spots on the array, seen in Figure 4, and are discussed further in Section 3.3. The remaining 1% of the pixels are non-responsive or very high dark current ‘bad’ pixels, and are more apparent in Figure 9.

#### 3.3 Linearity

The average of all the normal pixels for different exposure times is plotted in Figure 5. The straight line is a linear fit to the low exposure data to highlight deviations at the longer exposure times. The response is linear

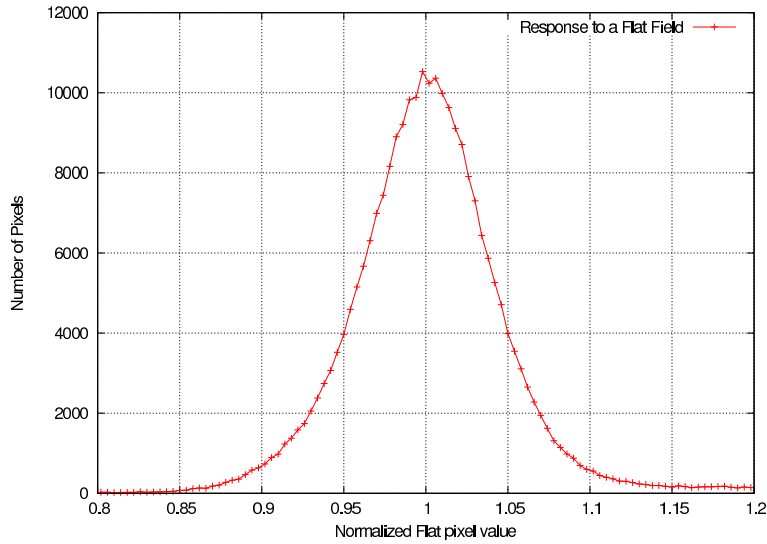


Figure 3. The histogram shown above is of the pixel response in the raw flat field image from Figure 4. Two histograms shown are due to two different attempts at illumination correction of the flat field by fitting a 2nd-order polynomial surface to the image. The pixel response has a spread of about 8%.

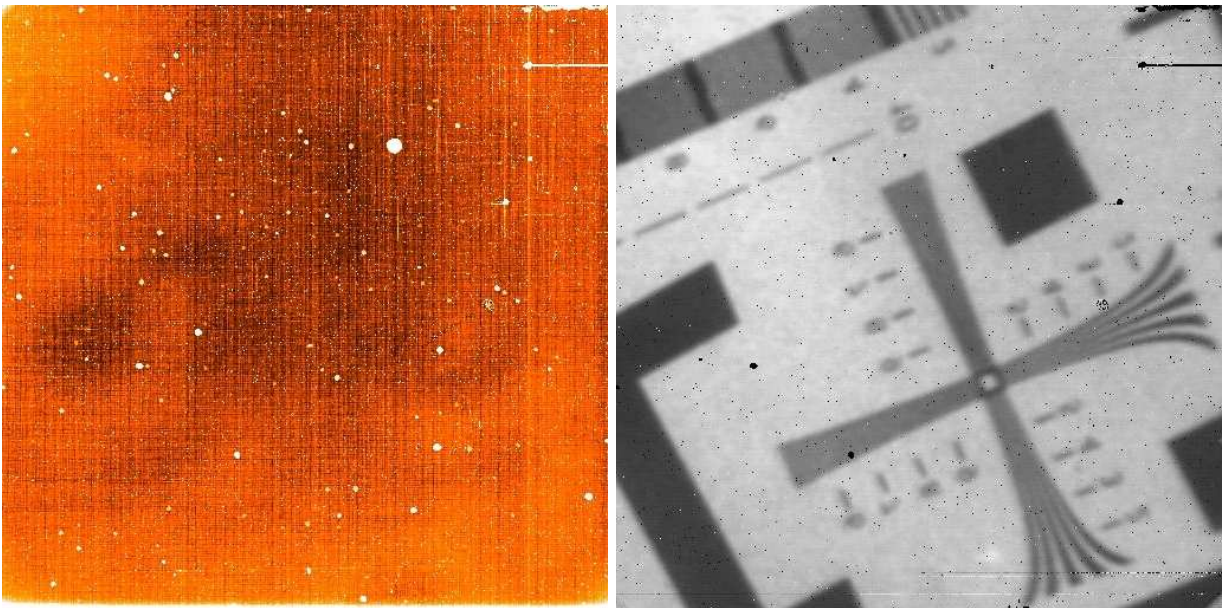


Figure 4. Shown above is an unprocessed flat field image from the InGaAs array at a reverse bias of 400mV across the pixels. Most of the circular spots are not dead, but respond in a different manner as shown in Figure 6. The picture on the right is a flat-corrected image of a scene focused on the array using a single bi-convex lens. The scene is slightly out of focus. Although the spots calibrate in a different manner, most of the features seen in the flat field image on the left calibrate out very well.

to within 1% for about 70% of the full-well capacity of the detector. By 80% of full well the deviation from linearity is 3%.

The array is sprinkled with numerous spots of varying size that are sensitive to light (Figure 4). The pixels in these spots respond differently from the normal pixels. While their response is linear, as seen in Figure 6, all the pixels in each spot seem to show the same ADU value to a degree that surpasses photon statistics. The

linearity in the pixels also seems to extend to a much larger range than normal pixels. This suggests that due to some form of bonding or doping defect, these pixels alike as a super-pixel. These super-pixels calibrate well as an average, as can be inferred by the near disappearance of the spots in the image on the right in Figure 4. However, spatial information within the super-pixels is lost.

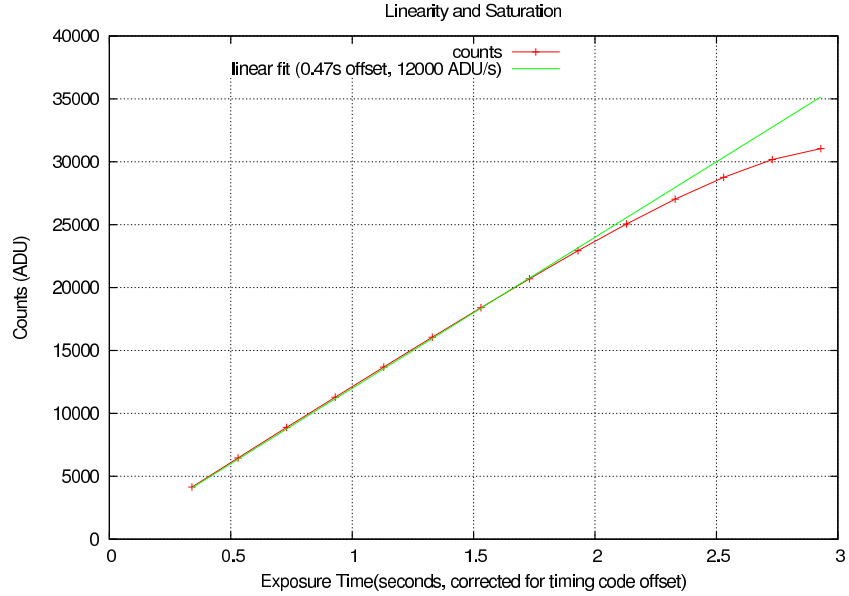


Figure 5. The array response is linear to about 70% of full-well. These measurements were obtained at a bias of -500mV and a corresponding gain of  $4.5e^-/ADU$ .

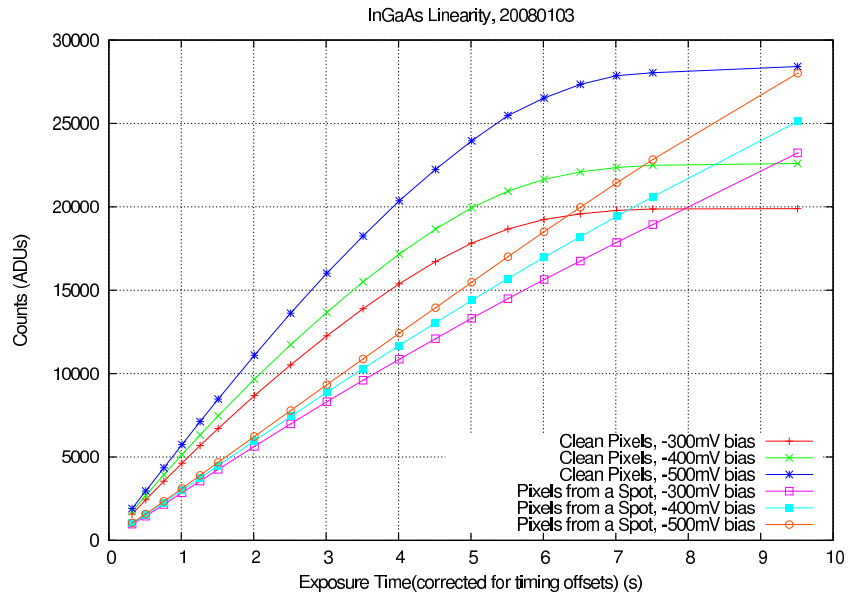


Figure 6. The linearity estimation for the spots shown in Figure 4 has also been calculated. At first look, the pixels in the spots look like they have a larger full-well range in ADUs as well as a larger gain.

### 3.4 Gain

Gain for the array has been estimated at  $4.5 \text{ e}^-/\text{ADU}$  for a bias of  $-500\text{mV}$ . This translates to a full well capacity of  $145,000 \text{ e}^-$ . Linear response is seen for up to  $100,000 \text{ e}^-$  of that capacity. These statistics are comparable to the capacity of commonly used near-infrared detectors in Astronomy.

The system noise has been estimated from the deviation of measured noise over photon noise at low levels of illumination. At zero-flux the RMS noise is estimated to be  $14.5\text{ADU}$  or  $65 \text{ e}^- \text{rms}$ . Pattern noise is apparent in the array images, and it is likely that the RMS noise is dominated by systematics arising from the electronic configuration rather than the intrinsic read noise of the device. SB-206 based devices operated in the astronomical community have read noises as low as  $\sim 20\text{e}^-$ .

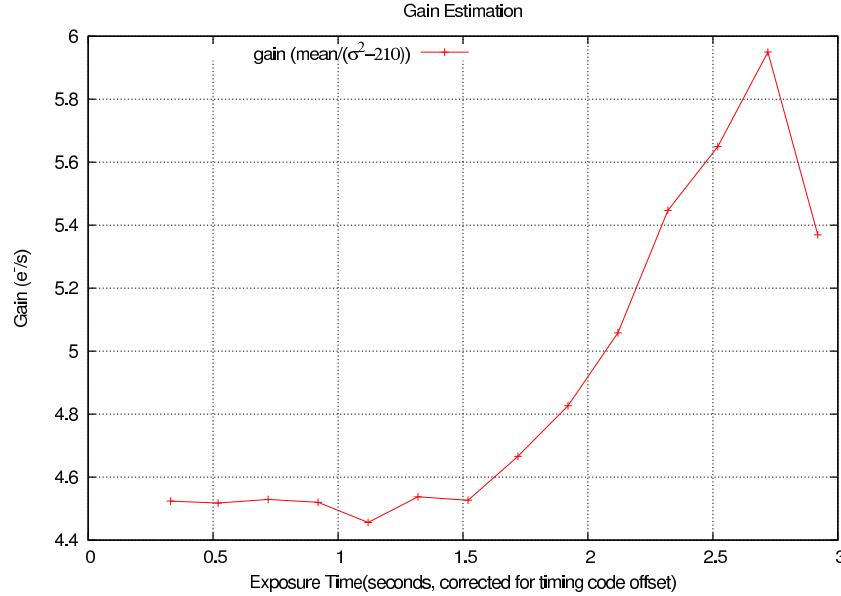


Figure 7. The gain is calculated from photon statistics. The rise in gain at higher exposure times is spurious and is an artifact created by the nonlinearity of the array response at higher ADUs.

### 3.5 Dark Current

For the dark current measurements, all apertures in the system cold shield and the aperture directly over the array were blocked off. The array was cooled to the system’s lowest temperature, then the cooling system was turned off and monitoring of dark current began. At this point the array temperature was  $80\text{K}$ . Measurements continued until dark current pushed the array into the non-linear regime in the shortest exposures. This typically happens at about  $150\text{K}$  for all the extended wavelength InGaAs detectors we have tested.

The dark current measurements are shown in the form of an Arrhenius plot in Figure 8. The values deviate from a straight line at lower temperatures as secondary, non-emission-capture model phenomena start to dominate dark current production. Of particular interest is the elevated dark current levels seen at the lowest temperatures (at the beginning of the warm-up, just after the cryocooler has been shut off). We have seen this feature<sup>7</sup> in the dark current measurements of arrays using two ROICs of different designs, both of which were tested using the closed-cycle cooling setup. However, we did not see a similar feature in our testing of diodes made with the same growth process, which were tested in a  $\text{LN}_2$  cooled dewar. This leads us to suspect that the elevated dark current signal at low temperatures is caused by emission from some relatively hot, unshielded portion of the cooler coils which equilibriate with the rest of the system after the cooler is turned off.

Figure 9 shows a dark current image and a histogram of about 50% of the image. The dark current levels achieved have a median of  $2.6 \text{ e}^-/s$  - well below the levels required for the applications we have stated in Section 1. The salient features in the histogram are the tight distribution around the peak and the negligible high dark

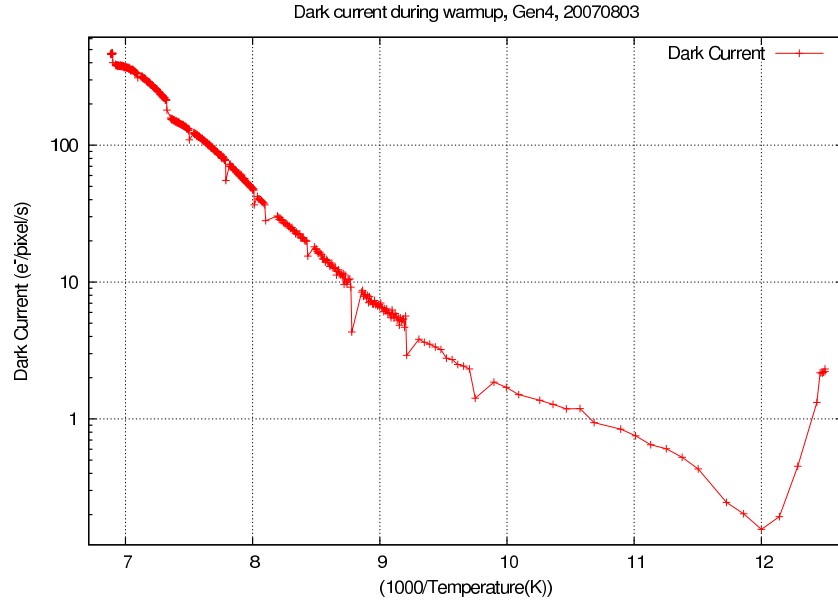


Figure 8. Dark current as a function of temperature. These measurements were done as the system warmed up after the refrigerator was turned off when at its coldest temperature.

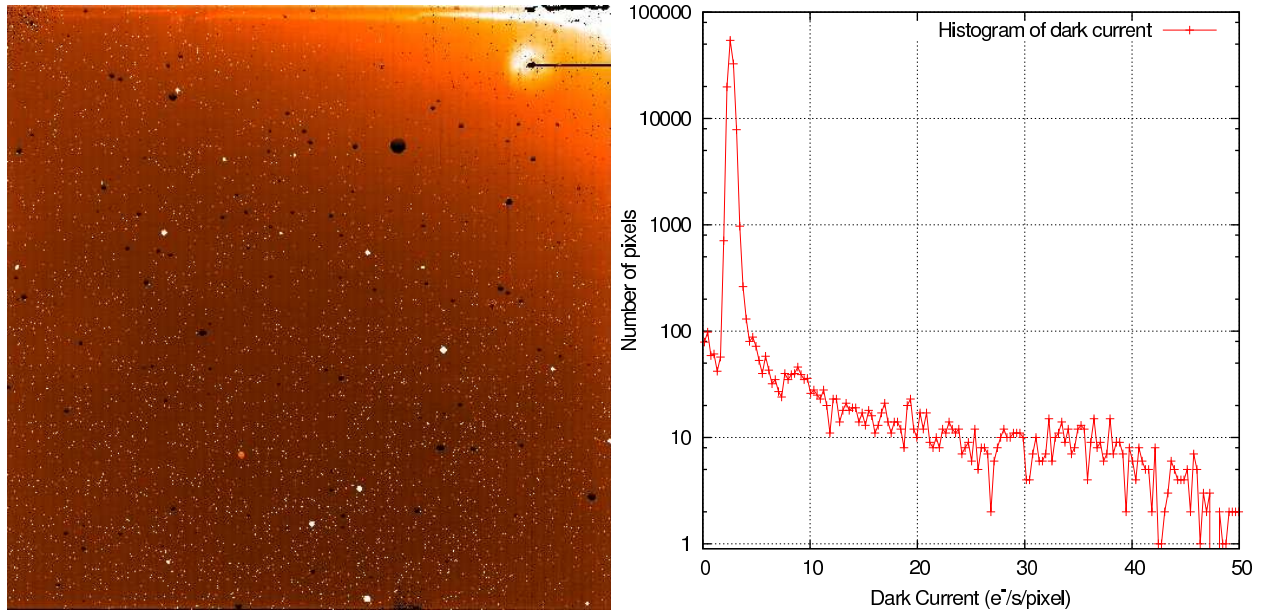


Figure 9. Shown above on the left is a median-combined image of twenty-five 300s dark exposures at a temperature of 80K. The white spots are all high dark current bad pixels, while the dark streaks on the top right are dead pixels. The dark circular spots are the peculiar features mentioned in Figure 4. The plot on the right is a histogram of dark current from the bottom 50% of the image on the left with a bin size of  $0.3 \text{ e}^-/\text{pixel/s}$ . The median dark current is  $2.6 \text{ e}^-/\text{pixel/s}$ .

current tail. We suspect that the dark current levels are lower than measured, and are being masked by the high read noise caused by the unresolved issues with regard to electrical shielding.

### 3.6 Spectral Quantum Efficiency Response

The quantum efficiency (QE) of the array was determined by making multiple measurements using the monochromator setup described in Section 2.4. A defocused spot, relayed from the monochromator, was imaged on the array and pixel values inside a box surrounding the image were subtracted from a similar box with no incident light. The ADU count was then converted to  $e^-$  using the gain calibration for the ROIC, and finally corrected for the integration time to derive a photo-electron rate at a given wavelength. This rate was calibrated by measuring the throughput of the monochromator setup using a reference InAs photodiode. As the diode would not allow for an automatic subtraction of ambient photon rate, the measurements included light-chopping by blinking the light source and acquiring a difference signal. The measurement for the diode is in  $Amp/s$ , which is converted to photo-electron rate. The measurement from the array is ratioed by this photo-electron rate to calibrate out the throughput of the monochromator and acquire the true spectral QE of the array.

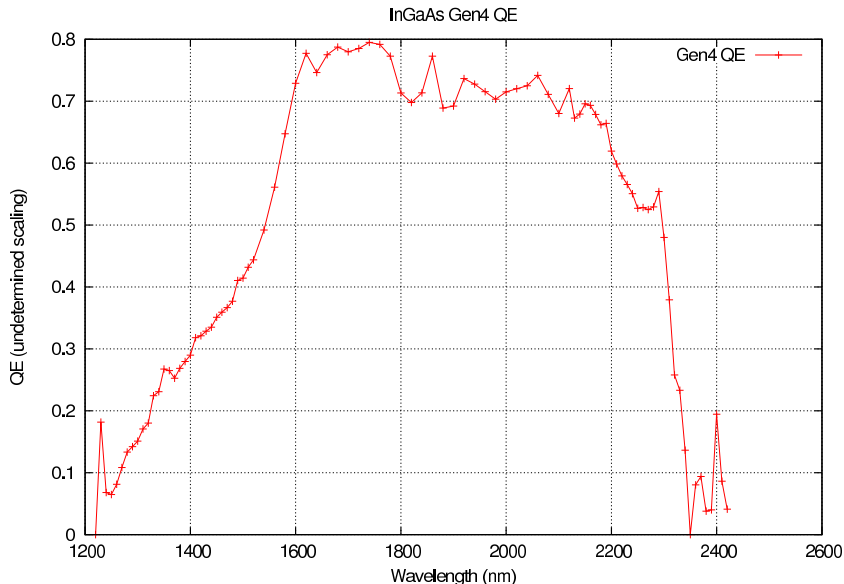


Figure 10. The spectral QE response of the InGaAs array. The noise in the QE measurement is due to a small mismatch between the array and calibrator diode wavelength calibration.

Results of QE measurements for the array are presented in Fig. 10. The QE is virtually identical to the values for the array based on a standard ROIC from GSU. Some noise can be seen in the measurement. This is due to a small mismatch between the wavelength calibration of the QE measurements for the array and the InAs reference photodiode. The 50% QE cutoff is at  $2320\text{ nm}$ , which lines up very closely with the long-wavelength cutoff of the  $K_s$  astronomical bandpass filter. The decline in QE at the shorter wavelengths is due to absorption in the buffer structure that makes the transition from the InP substrate to the extended wavelength InGaAs material.

## 4. DISCUSSION AND FUTURE

The arrays that have resulted from this project exceed all the requirements for broadband background-limited operation in the astronomical H and K-bands from the ground. The outstanding issues that affect operability are the high RMS-noise due to interference (Section 3.5) and the anomalous spots which respond differently from individual pixels (Section 3.3). We hope to resolve the noise issue by carefully managing the array wiring and grounding on the fanout board and cabling as we prepare to use this array in an astronomical instrument. The  $512 \times 512$  element SB-206 based array described here will be installed in CorMASS,<sup>10</sup> a cross-dispersed low-resolution ( $R=300$ ) spectrograph that currently disperses light from the  $0.8\text{-}2.5\mu\text{m}$  wavelength range in five spectral orders across an HgCdTe  $256 \times 256$  NICMOS3 array. CorMASS also includes a slit viewing mode in

which the array views the sky as a K-band imager. This instrument application will test the calibration and dark current performance of this array in a rigorous quantitative environment.

## ACKNOWLEDGMENTS

We acknowledge the support of this project by NSF grants AST-0352934 and AST-0605080, and are grateful for funding from a generous gift by the F.H Levinson Fund of the Peninsula Community Foundation.

## REFERENCES

- [1] Seshadri, S., Cole, D. M., Hancock, B., Ringold, P., Peay, C., Wrigley, C., Bonati, M., Brown, M. G., Schubnell, M., Rahmer, G., Guzman, D., Figer, D., Tarlé, G., Smith, R. M., and Bebek, C., “Characterization of NIR InGaAs imager arrays for the JDEM SNAP mission concept,” in [*High Energy, Optical, and Infrared Detectors for Astronomy II.*], Dorn, D. A. and Holland, A. D., eds., *Proceedings of the SPIE* **6276** (2006).
- [2] Brown, M. G., Bebek, C., Bernstein, G., Bonissent, A., Carithers, B., Cole, D., Figer, D., Gerdes, D., Gladney, L., Lorenzon, W., Kim, A., Kushner, G., Kuznetsova, N., Lampton, M., Levi, M., Linder, E., McKee, S., Miquel, R., Mostek, N., Mufson, S., Perlmutter, S., Schubnell, M., Seshadri, S., Shukla, H., Smith, R., Stebbins, A., Stoughton, C., and Tarlé, G., “Development of NIR detectors and science-driven requirements for SNAP,” in [*Space Telescopes and Instrumentation I: Optical, Infrared, and Millimeter.*], Mather, J. C., MacEwen, H. A., and de Graauw, M. W. M., eds., *Proceedings of the SPIE* **6265** (2006).
- [3] Gillett, F. C., “Infrared Arrays for Astronomy,” in [*Infrared Detectors and Instrumentation for Astronomy*], Fowler, A. M., ed., *Proceedings of the SPIE* **2475**, 2–7 (1995).
- [4] Gillett, F. C. and Mountain, M., “On the Comparative Performance of an 8 m NGST and a Ground Based 8 m Optical/IR Telescope,” in [*Science with the NGST*], Smith, E. P. and Korathor, A., eds., *ASP Conference Series* **133**, 42–51 (1998).
- [5] Linga, K. R., Olsen, G. H., Ban, V. S., Joshi, A. M., and Kosonocky, W. F., “Dark Current Analysis and Characterization of  $\text{In}_x\text{Ga}_{1-x}\text{As}/\text{InAs}_y\text{P}_{1-y}$  Graded Photodiodes with  $x > 0.53$  for Response to Longer Wavelengths ( $> 1.7\mu\text{m}$ ),” *Journal of Lightwave Technology* **10**, 1050–1055 (1992).
- [6] Linga, K. R., [*Ph.D. Thesis*], New Jersey Institute of Technology (1997).
- [7] Nelson, M. J., Skrutskie, M. F., Kanneganti, S., Park, C., and Fox, O., “Development of Extended Wavelength Response InGaAs Detectors for Astronomical Applications,” in [*High Energy, Optical, and Infrared Detectors for Astronomy II.*], Dorn, D. A. and Holland, A. D., eds., *Proceedings of the SPIE* **6276** (2006).
- [8] [*Aladdin 1024×1024 IRFPA User’s Guide*], Ratheon Vision Systems (2006).
- [9] [*ARC-42 Eight Channel IR Video Board User’s Manual*], Astronomical Research Cameras (2007).
- [10] Wilson, J. C., Skrutskie, M. F., Colonno, M. R., Enos, A. T., Smith, J. D., Gizis, J. E., Monet, D. G., and Houck, J. R., “CorMASS: A Compact and Efficient Near-Infrared Spectrograph for Studying Low-Mass Objects,” *Proceedings of the Astronomical Society of the Pacific* **113**, 227–239 (2001).